science.sciencemag.org/content/365/6453/570/suppl/DC1

Supplementary Material for

Generation and manipulation of Schrödinger cat states in Rydberg atom arrays

A. Omran, H. Levine, A. Keesling, G. Semeghini, T. T. Wang, S. Ebadi, H. Bernien,
A. S. Zibrov, H. Pichler, S. Choi, J. Cui, M. Rossignolo, P. Rembold, S. Montangero,
T. Calarco, M. Endres, M. Greiner, V. Vuletić, M. D. Lukin*

*Corresponding author. E-mail: lukin@physics.harvard.edu

Published 9 August 2019, *Science* **365**, 570 (2019)
DOI: 10.1126/science.aax9743

This PDF file includes:

Materials and Methods
Figs. S1 to S9
Table S1
References

Supplementary materials

Materials and Methods

Figs. S1 to S9

Table S1

References *(36-55)*

Contents

1 Experimental setup

The Rydberg excitations are enabled by a two-color laser system at $420\,\mathrm{nm}$ and $1013\,\mathrm{nm}$ wavelength. The $420\,\mathrm{nm}$ light is derived from a frequency-doubled titanium sapphire laser (M Squared SolsTiS 4000 PSX F) locked to an ultrastable reference cavity (by Stable Laser Systems). The $1013\,\mathrm{nm}$ light is obtained from a high-power fiber amplifier (ALS-IR-1015-10-A-SP by Azur Light Systems). The seed light is derived from a Fabry-Pérot laser diode injection locked to an external cavity diode laser (CEL002 by MOGLabs) stabilized to the same reference cavity and filtered by the cavity transmission (*36*). The detuning of both Rydberg lasers to the intermediate state $\left|6P_{3/2}, F = 3, m_F = -3\right\rangle$ is approximately $2\pi \times 2\,\mathrm{GHz}$. The individual Rabi frequencies of the two Rydberg lasers are $\Omega_{420}/(2\pi) \approx 174\,\mathrm{MHz}$ and $\Omega_{1013}/(2\pi) \approx 115\,\mathrm{MHz}$. This gives a two-photon Rabi frequency of $\Omega = \Omega_{420}\Omega_{1013}/(2\Delta) \approx 2\pi \times 5\,\mathrm{MHz}$. We define the local phases of each atom's states $|0\rangle$ and $|1\rangle$ in the reference frame associated with the local phases of Rydberg excitation lasers, such that the two GHZ components have a relative phase $\phi = 0$ after state preparation.

To drive the optimal control pulses, we modulate the $420\,\mathrm{nm}$ Rydberg laser with an acousto-optic modulator (AOM) driven by an arbitrary waveform generator (AWG, M4i.6631-x8 by Spectrum). We correct the nonlinear response of the AOM to the drive amplitude by a feed-forward approach to obtain the target output intensity pattern. Furthermore, the AOM efficiency changes with changing frequency, which we compensate by feeding forward onto the waveform amplitude to suppress the intensity variations with frequency. In addition, the light shift on the Rydberg transition from the $420\,\mathrm{nm}$ laser can be as large as $2\pi \times 4\,\mathrm{MHz}$. While the pulse intensity changes, this light shift changes, modifying the detuning profile. We therefore correct the frequency profile as a function of the pulse intensity to compensate this shift. These steps ensure that the experimentally applied pulse is a faithful representation of the desired profile.

The local addressing beam patterns are generated by two AODs (DTSX400-800 by AA Opto-electronic), each driven by multiple frequencies obtained from an arbitrary waveform generator (M4i.6631-x8 by Spectrum).

2 Optimal control

Optimal control was originally developed as a tool to harness chemical reactions to obtain the largest amount of desired products with given resources, and then introduced in quantum information processing as a standard way of designing quantum protocols and quantum devices (*37–40*) as well as in manipulating quantum many-body systems to exploit complex phenomena (*26,41–49*). Quantum optimal control theory identifies the optimal shape of a time-dependent control pulse to drive a quantum many-body system to accomplish given task, e.g. state preparation or quantum gate implementation. The quality of the transformation is certified by a Figure of Merit (FoM) that can be calculated or measured, e.g. the fidelity of the final state with respect to the target one, the final occupation, or the energy.

In this work, the optimization is achieved through RedCRAB, the remote version of the dressed Chopped RAndom Basis (dCRAB) optimal control via a cloud server (*26, 41, 48*). Within the optimization, control fields such as the Rabi coupling $\Omega(t)$ are adjusted as $\Omega(t) = \Omega_0(t) + f(t)$, where $\Omega_0(t)$ is an initial guess function obtained from physical intuition or existing suboptimal solutions. The correcting function $f(t)$ is expanded by randomized basis functions. In this work, we chose a truncated Fourier basis. Thus, $f(t) = \Gamma(t) \sum_{k=1}^{n_c} [A_k \sin(\omega_k t) + B_k \cos(\omega_k t)]$, where $\omega_k = 2\pi(k+r_k)/\tau$ are randomized Fourier frequencies with $r_k \in [-0.5, 0.5]$, τ is the final time, and $\Gamma(t)$ is a fixed scaling function to keep the values at initial and final times unchanged, i.e., $\Gamma(0) = \Gamma(\tau) = 0$. The optimization task is then translated into a search for the optimal combination of $\{A_k, B_k\}$ with a given r_k to maximize the fidelity between the target state and the time evolved state at τ. It can be solved by iteratively updating $\{A_k, B_k\}$ using a standard Nelder-Mead algorithm (*50*). In the basic version of the CRAB algorithm, all r_k are fixed and the local control landscape is explored for all n_c frequencies simultaneously. This leads to a restriction in the number of frequencies that can be efficiently optimised. Using the dressed CRAB (dCRAB) algorithm, only one Fourier frequency ω_k is optimised at a time. We then move on to ω_{k+1} after a certain number of iterations of the CRAB routine. This enables the method to include an arbitrarily large number of Fourier components and deriving the solutions without – whenever no other constraints are present – being trapped by local optima (*25*).

In the RedCRAB optimization, the server generates and transmits a trial set of controls to the client user, who will then evaluate the corresponding FoM and communicates the feedback information to the server finishing one iteration loop (Fig. S1). The optimization continues iteratively and the optimal set of controls, as well as the corresponding FoM are derived. In the RedCRAB optimization, the user can either evaluate the FoM by numerical calculation, namely open-loop optimization, or by experimental measurement, which is called closed-loop optimization. In this work, open-loop optimization was carried out only. The resulting controls could later serve as the initial guess for a future closed-loop optimization. This last step would ensure that the resulting controls are robust, since all unknown or not modelled experimental defects and perturbations would automatically be corrected for.

For the open-loop optimization of the pulse, we constrained the preparation time to $1.1\,\mu$s and allowed the detuning $\Delta/(2\pi)$ to vary between $-20\,$MHz and $20\,$MHz, while $\Omega/(2\pi)$ could vary between $0-5\,$MHz. The resulting pulses are shown in Fig. S2. While shorter pulses can work sufficiently well for smaller system sizes, we use an equal pulse duration for all N for better comparability. We find that the optimized pulses for larger systems appear smoother than for smaller system sizes, where the pulses bear less resemblance to an adiabatic protocol. However, the adiabaticity does not improve for larger system sizes, owing to the shrinking energy gaps.

3 Optimal control dynamics

To gain insight into the timescales required to prepare a GHZ state in our setup, we can compare our optimal control protocol with a minimal quantum circuit consisting of a series of two-qubit gates that would achieve the same task. In this circuit, a Bell pair is created in the first layer $p = 1$ in the middle of the array using the Rydberg blockade, which for our maximal coupling strength of $\Omega/(2\pi) = 5\,\mathrm{MHz}$ takes $100\,\mathrm{ns}/\sqrt{2}$. The entanglement can be spread to the two atoms adjacent to this Bell pair by simultaneously applying a pair of local π pulses of $100\,\mathrm{ns}$ to those sites, corresponding to controlled rotations. A sequence of such gate layers $p = 2, ..., 10$, including operations on qubit pairs and the free evolution of other qubits, leads to the same GHZ state we prepare. This gate sequence requires approximately $1\,\mu$s, which is within 10% of the total evolution time required in our optimal control sequence, which builds up the entanglement in parallel. Furthermore, the fidelity of each layer of such a circuit effectively acting on all $N = 20$ qubits needs to be higher than 0.94 to achieve the 20-qubit GHZ fidelity demonstrated in this work.

It is interesting to compare this required evolution time with a parameter ramp that tries to adiabatically connect the initial state to the GHZ state. To this end, we parametrize the detuning and Rabi frequency as $\Delta(s) = (1 - s)\Delta_0 + s\Delta_1$ and $\Omega(s) = \Omega_{\mathrm{max}}[1 - \cos^{12}(\pi s)]$ respectively. A naïve (unoptimized) linear ramp of the detuning corresponds to choosing $s = t/T$. Alternatively, one can adjust the local ramp speed to minimize diabatic transitions, for example by choosing $s(t)$ minimizing

$$D = \left(\frac{ds}{dt}\right)^2 \sum_{n>0} \frac{|\langle E_n(s)|\partial_s H(s)|E_0(s)\rangle|^2}{(E_n(s) - E_0(s))^2}$$

during a ramp of duration T. Here $|E_n(s)\rangle$ are the instantaneous eigenstates of the Hamiltonian $H(s)$ specified by the parameters $\Omega(s)$ and $\Delta(s)$, with $|E_0(s)\rangle$ denoting the instantaneous ground state. In Figure S3, we show the results of numerical simulations using both the linear sweep and a sweep that minimizes the strength of diabatic processes quantified by D. Both sweep profiles require larger total evolution time T than the optimal control pulse to reach similar fidelities.

To understand the origin of the speedup through optimal control, we numerically simulate the corresponding evolution and analyze the population of the instantaneous energy eigenstates (Fig. S4). The optimal control dynamics can be divided into three different regions: (I) A fast initial quench, (II) a slow quench, and (III) a fast final quench. Even though the change in the Hamiltonian parameters in region (I) is rather rapid, the system remains mostly in the instantaneous ground state, with negligible populations of the exited states, since the energy gap is large. In contrast, in region (II) the parameters change slows down, reflecting the fact that the energy gap becomes minimal. Unlike the adiabatic case however, one can observe nontrivial population dynamics, with a temporary population of excited states. Importantly, the optimal control finds a path in the parameter space such that the population is mostly recaptured in the ground state at the end of region (II). Finally, in region (III) the gap is large again and the system parameters are quickly changed to correct also for higher order contributions. This suggests that it actively uses diabatic transitions that go beyond the adiabatic principle. This mechanism is related to the recently discussed speedup in the context of the quantum approximate optimization algorithm (QAOA) (*30, 31*).

4 Quantifying detection

The many-body dynamics involving coherent excitation to Rydberg states occurs during a few-microsecond time window in which the optical tweezers are turned off. After the coherent dynamics, the tweezers are turned back on, and atoms in the ground state $|0\rangle$ are recaptured. However, there is a small but finite chance of losing these atoms. To quantify this error, we perform the GHZ state preparation experiment while disabling the $420\,\mathrm{nm}$ Rydberg pulse. This keeps all atoms in state $|0\rangle$, and we measure the loss probability to find a $0.9937(1)$ detection fidelity.

Atoms in state $|1\rangle$ on the other hand have a small chance of being misidentified as being in state $|0\rangle$, as these atoms can decay prematurely from the Rydberg state to the ground state and get recaptured by the tweezers. This error probability can be measured by preparing atoms at sufficiently large distances as to be non-interacting and applying a calibrated π pulse to transfer all atoms to $|1\rangle$ and measure the probability of recapturing them. However, part of this signal is given by the π pulse infidelity, i.e. a small fraction of atoms which did not get excited to $|1\rangle$ in the first place.

To quantify the π pulse fidelity, we note that a Rydberg atom that decays and is recaptured can decay either into the $F = 2$ or $F = 1$ ground states with branching ratios α and β, respectively ($\alpha + \beta = 1$). Our initial optical pumping of atoms into $|0\rangle$ has high fidelity > 0.998, measured using microwave spectroscopy on different sublevels of the $F = 2$ manifold. Thus, the final population of $F = 1$ atoms should be given only by Rydberg atom decay/recapture events. Following a π pulse to excite all atoms to the Rydberg state, the final measured population in $F = 1$ is $p_1 = p \times \beta$, where p is the total decay and recapture probability of a Rydberg atom. Meanwhile, the final measured population in $F = 2$ is $p_2 = p \times \alpha + \epsilon$, which includes both decay events from Rydberg atoms as well as residual population ϵ left from an imperfect π pulse. Experimentally, we separately measure the total recaptured ground state population $(p_1 + p_2)$, as well as the $F = 1$ population p_1 only (by a resonant push-out of $F = 2$ atoms). We additionally can vary the overall recapture probability p by changing the depth of the tweezers that we recapture atoms in, which changes the repulsive force exerted by the optical tweezers on Rydberg atoms (*28*). We measure p_1 and $(p_1 + p_2)$ at four different total recapture probabilities to extract the π pulse infidelity as $\epsilon = 0.006(3)$ (Fig. S5). From these measurements, we conclude a Rydberg detection fidelity of $0.9773(42)$.

Detection errors of $|0\rangle$ can be mitigated by implementing ground-state cooling in the tweezers (*51, 52*), which reduces the probability of loss after releasing the atoms. The detection fidelity of $|1\rangle$ can be improved by using Rydberg states with a longer radiative lifetime, actively ionizing the Rydberg atoms by electric or optical fields, or by pulling them away from the trapping region with electric field gradients.

5 Accounting for detection imperfections

The small imperfections in state detection of single qubits leads to a prominent effect on the analysis of large systems. The probability for a single detection error is sufficiently low that multiple errors per chain are very unlikely, and we observe that the reduction in probability of observing the correct GHZ pattern is dominated by these errors, as opposed to excitations of the system (Fig. S6A). This conclusion is further confirmed by noting that near-ideal correlations extend across the entire system (Fig. S7).

To properly infer the obtained fidelities, we account for these imperfections using the following procedure:

Coherences: The coherences are extracted from the amplitude of parity oscillations. Each point in the parity oscillation is analyzed from the measured distribution of the number of excitations in the system. We encode this measured probability distribution in the vector $\mathbf{W}$, where W_n is the probability to observe exactly n excitations in the system ($0 \leq n \leq N$). The true probability distribution of excitation numbers, prior to the effect of detection errors, is denoted $\mathbf{V}$. Detection errors transform this distribution according to a matrix M, where M_{mn} encodes the probability that a state with n excitations will be detected as having m excitations. Each matrix element is calculated using combinatoric arguments from the measured detection fidelities. We determine the true distribution $\mathbf{V}$ as the one that minimizes the cost function $|M\mathbf{V} - \mathbf{W}|^2$. (Fig. S6B). This procedure is similar to applying the inverse matrix M^{-1} to the measured distribution $\mathbf{W}$, but is more robust in the presence of statistical noise on the measured distribution. Error bars on the inferred values are evaluated by random sampling of detection fidelities, given our measured values and uncertainties.

Populations: We carry out a similar procedure for the population data; however, we are interested in assessing the probability of two particular target states, which are defined not only by their number of excitations but also by their staggered magnetizations $M_n = \sum_{i=1}^{N} (-1)^i \langle \sigma_z^{(i)} \rangle$. Our procedure therefore operates by grouping all possible microstates according to their common staggered magnetization and number of excitations (Fig. S6C). For N particles, there are in general $(N/2+1)^2$ such groups. As before, we denote the raw measured distribution with respect to these groups as $\mathbf{W}$. We construct a detection error matrix M that redistributes populations between groups according to the measured detection error rates. We optimize over all possible true distributions to find the inferred distribution $\mathbf{V}$ that minimizes the cost function $|M\mathbf{V} - \mathbf{W}|^2$. Following this procedure, we sum the populations in the two groups that uniquely define the two target GHZ components with a staggered magnetization of $\pm N$, and $N/2$ excitations.

6 Bounding the GHZ state coherence

We expand an experimental GHZ-like density matrix in the following form

$$\rho = \alpha_1 \left|A_N\right\rangle\!\left\langle A_N\right| + \alpha_2 \left|\overline{A}_N\right\rangle\!\left\langle\overline{A}_N\right| + \left(\beta \left|A_N\right\rangle\!\left\langle\overline{A}_N\right| + \beta^* \left|\overline{A}_N\right\rangle\!\left\langle A_N\right|\right) + \rho' \tag{1}$$

where $|A_N\rangle = |0101\cdots\rangle$ and $\left|\overline{A}_N\right\rangle = |1010\cdots\rangle$ are the target GHZ components, α_i characterizes the diagonal populations in these states $(0 \leq \alpha_i \leq 1)$, β characterizes the off-diagonal coherence between these states $(0 \leq |\beta| \leq 1/2)$, and ρ' contains all other parts of the density matrix. The GHZ fidelity of state ρ is given by:

$$\mathcal{F} = \langle \mathrm{GHZ}_N | \, \rho \, | \mathrm{GHZ}_N \rangle = \frac{\alpha_1 + \alpha_2}{2} + \mathrm{Re}(\beta) \tag{2}$$

To measure the coherence $|\beta|$, we implement a staggered magnetic field to which the target GHZ state is maximally sensitive:

$$H_{\text{st}} = \frac{\hbar\delta}{2}\sum_{i=1}^{N}(-1)^i \sigma_z^{(i)} \tag{3}$$

Applying H_{st} to the system for time T results in unitary phase accumulation $U(T) = \exp\left(-iH_{\text{st}}T/\hbar\right)$. We then apply a unitary $\mathcal{U}$ to the system and measure in the computational basis. From repeated measurements, we calculate the expectation value of the global parity operator $\mathcal{P} = \prod_i \sigma_z^{(i)}$ as a function of the phase accumulation time T. Denote the time-dependent expectation value $E(T)$, where $-1 \leq E(T) \leq 1$.

We show that if $E(T)$ has a frequency component that oscillates at a frequency of $N\delta$, then the amplitude of this frequency component sets a lower bound for $|\beta|$. Importantly, this holds for any unitary $\mathcal{U}$ used to detect the phase accumulation.

Proof: The expectation value $E(T)$ can be written explicitly as the expectation value of the time-evolved observable $\mathcal{P} \to U^\dagger(T)\mathcal{U}^\dagger\mathcal{P}\mathcal{U}U(T)$. In particular,

$$E(T) = \text{Tr}[\rho U^\dagger(T)\mathcal{U}^\dagger\mathcal{P}\mathcal{U}U(T)] = \sum_n \langle n|\, \rho U^\dagger(T)\mathcal{U}^\dagger\mathcal{P}\mathcal{U}U(T)\, |n\rangle \tag{4}$$

where $|n\rangle$ labels all computational basis states. Since the phase accumulation Hamiltonian H_{st} is diagonal in the computational basis, the basis states $|n\rangle$ are eigenvectors of $U(T)$ with eigenvalues denoting the phase accumulation. Specifically,

$$H_{\text{st}}\,|n\rangle = \frac{\hbar\delta}{2}M_n\,|n\rangle \Rightarrow U(T)\,|n\rangle = e^{-i\delta T M_n/2}\,|n\rangle \tag{5}$$

where M_n is the staggered magnetization of state $|n\rangle$ defined earlier. The staggered magnetization of the state $|A_N\rangle$ is maximal: $M_{A_N} = N$, and the staggered magnetization of $\left|\overline{A}_N\right\rangle$ is minimal: $M_{\overline{A}_N} = -N$. Note that all other computational basis states have strictly smaller staggered magnetizations. Inserting an identity operator in Eq. (4):

$$E(T) = \sum_{n,m} \langle n| \rho |m\rangle\langle m| U(T)^\dagger \mathcal{U}^\dagger \mathcal{P} \mathcal{U} U(T) |n\rangle = \sum_{n,m} e^{-i\delta T(M_n - M_m)/2} \langle n| \rho |m\rangle\langle m| \mathcal{U}^\dagger \mathcal{P} \mathcal{U} |n\rangle \tag{6}$$

The highest frequency component comes from the states with maximally separated staggered magnetization, $|n\rangle = |A_n\rangle$ and $|m\rangle = \left|\overline{A}_n\right\rangle$. Separating out this frequency component as $F(T)$, we obtain:

$$F(T) = 2\mathrm{Re}\left[e^{-iN\delta T} \langle A_N| \rho \left|\overline{A}_N\right\rangle\left\langle\overline{A}_N\right| \mathcal{U}^\dagger \mathcal{P} \mathcal{U} |A_N\rangle\right] = 2\mathrm{Re}\left[\beta e^{-iN\delta T} \left\langle\overline{A}_N\right| \mathcal{U}^\dagger \mathcal{P} \mathcal{U} |A_N\rangle\right] \tag{7}$$

We note that the parity matrix element is bounded as $0 \leq \left|\langle\overline{A}_N|\mathcal{U}^\dagger \mathcal{P} \mathcal{U}|A_N\rangle\right| \leq 1$. Furthermore, the matrix element is real-valued and positive for the unitary $\mathcal{U}$ considered in the experiment. Fitting $F(T)$ to an oscillation with amplitude $C \geq 0$ and phase ϕ according to $F(T) = C\cos(N\delta T - \phi)$, we produce our lower bound for the off-diagonal coherence β:

$$|\beta| \geq C/2; \quad \arg(\beta) = \phi \tag{8}$$

7 Parity detection

The ideal observable to measure GHZ phase is the parity $\mathcal{P}_x = \prod_i \sigma_x^{(i)}$. However, the presence of Rydberg interactions and the Rydberg blockade prevents us from rotating all qubits such that we can measure in this basis. Instead, in this work we generate a unitary $\mathcal{U}_x = \exp\left(-i\Omega t/2 \sum_i \sigma_x^{(i)} - iH_{\mathrm{int}} t/\hbar\right)$ by resonantly driving all atoms in the presence of these interactions given by H_{int} for a fixed, optimized time (Fig. S8), and subsequently measure the parity $\mathcal{P} = \prod_i \sigma_z^{(i)}$ in the computational basis. The finite duration of the unitary $\mathcal{U}_x$ incurs a small amount of additional infidelity, owing both to dephasing and an additional laser scattering. However, we estimate that this effect should only lead to small losses in fidelity on the percent level.

While it is not obvious that the parity observable used here is suitable, we can understand the parity oscillations in the picture of weakly interacting spin-1 particles defined on dimers of neighboring pairs of sites. For two adjacent sites, we can define eigenstates of a spin-1 S_z operator as $|\circ\bullet\rangle = |-\rangle$, $|\circ\circ\rangle = |0\rangle$, and $|\bullet\circ\rangle = |+\rangle$. In this notation, the antiferromagnetic GHZ state we prepare is given by a ferromagnetic GHZ state in the spin-1 basis:

$$|\mathrm{GHZ}_N\rangle = \frac{1}{\sqrt{2}}\left(|+++\cdots\rangle + |---\cdots\rangle\right) \tag{9}$$

We must express all operations on the GHZ state in this new notation. In particular, the transverse field of the form $\hbar\Omega/2\sum_i \sigma_x^{(i)}$ applied to individual atoms gets transformed to an operation $\hbar\Omega/\sqrt{2}\sum_j S_x^{(j)}$ on all dimers. Furthermore, the staggered field $\hbar\delta/2\sum_i(-1)^i\sigma_z^{(i)}$ we apply to individual atoms to rotate the GHZ phase is equivalent to an operation of the form $\hbar\delta\sum_j S_z^{(j)}$ acting on individual dimers.

The parity operator in the single-qubit basis $\mathcal{P} = \prod_i \sigma_z^{(i)}$ can be transformed into the dimer basis as

$$\mathcal{P} = \prod_j \left(-\,|+\rangle\langle+|_j - |-\rangle\langle-|_j + |0\rangle\langle 0|_j\right) \tag{10}$$

by noting that the three dimer states are eigenstates of $\mathcal{P}$, i.e. $\mathcal{P}\,|\pm\rangle = -\,|\pm\rangle$ and $\mathcal{P}\,|0\rangle = |0\rangle$.

Assuming we begin from a GHZ state, applying a rotation on all dimers for a duration given by $\Omega t = \pi/\sqrt{2}$ saturates the difference in $\mathcal{P}$ between GHZ states of opposite phase. This shows that such a protocol would be optimal if the dimer approximation were exact. However, interactions between dimers cannot be neglected. In particular, the Rydberg blockade suppresses configurations of the form $|\cdots -+\cdots\rangle$ owing to the strong nearest-neighbor interaction V, and neighboring dimers of the same type such as $|\cdots \pm\pm\cdots\rangle$ have a weak interaction given by the next-to-nearest neighbor interaction strength $V_2 = V/2^6$. We can thus express the interactions in the system as

$$\frac{H_{\mathrm{int}}}{\hbar} = \sum_{j=1}^{N/2-1} V_2\,|+\rangle\langle+|_j\,|+\rangle\langle+|_{j+1} + V_2\,|-\rangle\langle-|_j\,|-\rangle\langle-|_{j+1} + V\,|-\rangle\langle-|_j\,|+\rangle\langle+|_{j+1} \tag{11}$$

An exact simulation of the dimer rotation under the interaction Hamiltonian (11) shows that both these interaction effects reduce the parity contrast by a small amount. In the recently discussed context of quantum many-body scars (*20, 32, 53, 54*), these effects of residual interactions lead of small deviations from a stable periodic trajectory through phase space.

8 Staggered field calibration

To apply the staggered field (3), we address each of the even sites in the array with a focused off-resonant laser beam at $420\,\mathrm{nm}$. However, the unitary in question requires a staggered field with opposite sign on every site. We compensate for the missing acquired phase on the sites in between the addressed ones by shifting the phase of the Rydberg laser, through a change in phase of the radio-frequency drive of the AOM. The intensity of each addressing beam is measured by applying a spin-echo sequence with an addressing pulse of variable duration to determine the light shift on the Rydberg transition. We correct for inhomogeneous intensities so that all atoms are subject to the same light shift.

We measure and calibrate the staggered field by measuring the effect of the field on each atom individually. To do so, we alternately rearrange the atoms to form different subsets of the 20-atom system that are sufficiently far apart to avoid interactions between them. In this configuration, every atom is then subject to a $\pi/2$ rotation about the x-axis, followed by the staggered field for variable duration, then a $\pi/2$ rotation about the y-axis, to distinguish positive from negative phase evolution. With an additional π rotation about the y-axis, we perform a spin echo to mitigate effects of dephasing. The outcome of this protocol is shown in Fig. S9 and demonstrates the implementation of the staggered magnetic field. By switching the local addressing beams to the opposite set of alternating sites, we switch the sign of the staggered field, enabling the measurement of both positive and negative phase accumulation.

9 Measured GHZ fidelities

For each system size N, we measure the GHZ populations and the GHZ coherence by parity oscillations (Figs. 2, 3 of the main text). From the raw measurements, we infer the true GHZ fidelity using the maximum likelihood procedure discussed in Section 5. All measured values are shown in table S1. Error bars on raw populations represent a 68% confidence interval for the measured value. Error bars on the raw coherences are fit uncertainties from the parity oscillations. Error bars on the inferred values include propagation of the uncertainty in the estimation of the detection fidelities.

10 Experimental Imperfections

We identify a number of experimental imperfections that to varying degrees can limit the coherent control of our atomic system.

1. **Atomic temperature:** The atom temperature of $\sim 10\,\mu$K leads to fluctuating Doppler shifts in the addressing lasers of order $\sim 2\pi \times 43$ kHz, as well as fluctuations in atomic position that leads to variation in Rydberg interactions strengths. These fluctuations are included in the simulations shown in the main text Figure 3. These effects can be dramatically reduced by improved atomic cooling, most notably by sideband cooling within the optical tweezers to the motional ground state (*51, 52*).

2. **Laser scattering:** The two-photon excitation scheme to our chosen Rydberg state leads to off-resonant scattering from the intermediate state, $6P_{3/2}$. This scattering rate has a timescale of $50 - 100\mu$s for the two laser fields, and can be reduced by higher laser powers and further detuning from the intermediate state.

3. **Rydberg state lifetime:** The $70S$ Rydberg state has an estimated lifetime of $150\ \mu$s (*55*),

limited both by radiative decay and blackbody-stimulated transitions. This effect could be mitigated by selecting a higher Rydberg state with a longer lifetime or by cryogenic cooling of the blackbody environment.

Additional error sources that may limit our coherence properties include laser phase noise, which can be mitigated by better laser sources and stabilization schemes, and fluctuations in local addressing beam intensities and positions, which can be addressed by active feedback on the beam positions and improved thermal and mechanical stability of the setup. Simulations predict that we could go beyond the system sizes studied here. While GHZ states of $N = 24$ could be within reach with current parameters, generation of even larger GHZ states should be feasible with the additional technical improvements discussed above.

11 Ground-state qubit encoding

The GHZ state parity could be more easily detected and manipulated if the qubits were encoded in a basis of hyperfine sublevels of the electronic ground state. In particular, one can consider two alternative qubit states $|\tilde{0}\rangle = \left|5S_{1/2}, F = 1, m_F = -1\right\rangle$ and $|\tilde{1}\rangle = \left|5S_{1/2}, F = 2, m_F = -2\right\rangle$. Rotations between these states are possible through stimulated Raman transitions or microwave driving, and the interactions are introduced by coupling $|\tilde{1}\rangle$ to a Rydberg level $|r\rangle$. This type of hyperfine encoding has been employed in multiple experiments with cold Rydberg atoms (*22, 23, 33*). To prepare GHZ states in this basis, all atoms can be initialized in $|\tilde{1}\rangle$ and the system transferred to the state $|\tilde{1}r\tilde{1}r\cdots\rangle + |r\tilde{1}r\tilde{1}\cdots\rangle$ using the method described in this work. A ground-state qubit π pulse followed by a π pulse on the Rydberg transition transforms the state into $|\tilde{0}\tilde{1}\tilde{0}\tilde{1}\cdots\rangle + |\tilde{1}\tilde{0}\tilde{1}\tilde{0}\cdots\rangle$, enabling the long-lived storage of entanglement. Additionally, local qubit rotations can flip the state of every other site to prepare the canonical form of the GHZ state, $|\tilde{0}\tilde{0}\tilde{0}\cdots\rangle + |\tilde{1}\tilde{1}\tilde{1}\cdots\rangle$, which can achieve entanglement-enhanced metrological sensitivity to homogeneous external fields (*2*). Incorporating this type of hyperfine qubit encoding with Rydberg qubit control will be important for realizing quantum gates and deeper quantum circuits in future experiments.

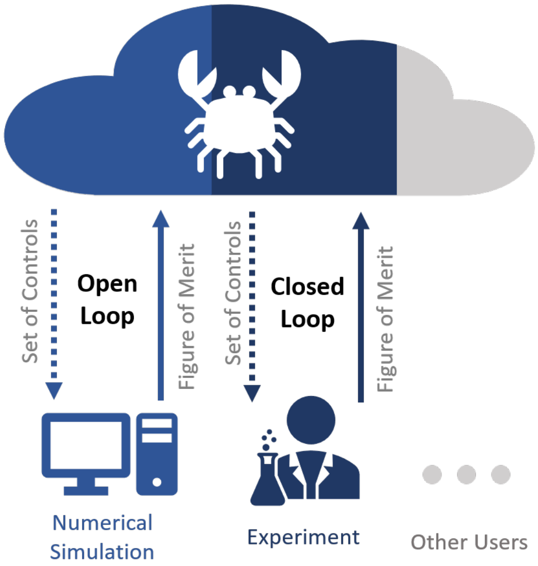

Figure S1: RedCRAB optimization loop. The remote dCRAB server generates and transmits a trial set of controls to the user, who evaluates the corresponding performance in terms of a FoM and sends the feedback information to the server, concluding one iteration loop. In the next loop, the server tends to generate an improved set of controls based on previous feedback information. The optimization continues until it converges. The FoM evaluation can be achieved either by numerical calculation (open-loop optimization) or experimental measurement (closed-loop optimization).

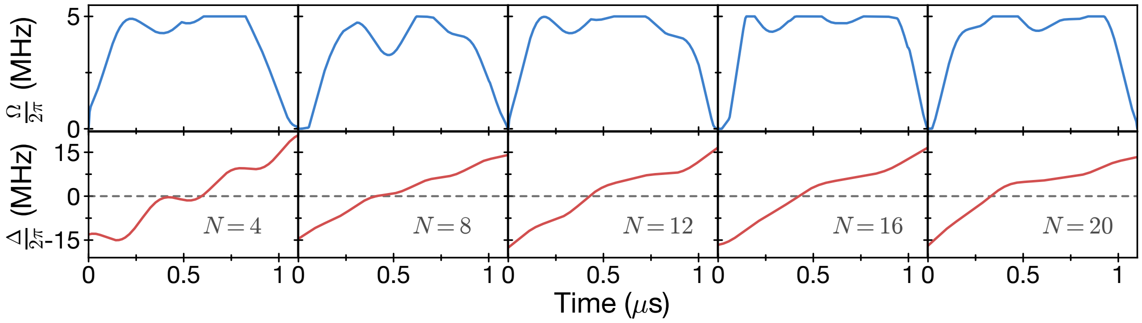

Figure S2: Optimal control pulse diagrams. Shown are the Rabi frequency (top) and detuning profiles (bottom) for the different system sizes investigated here.

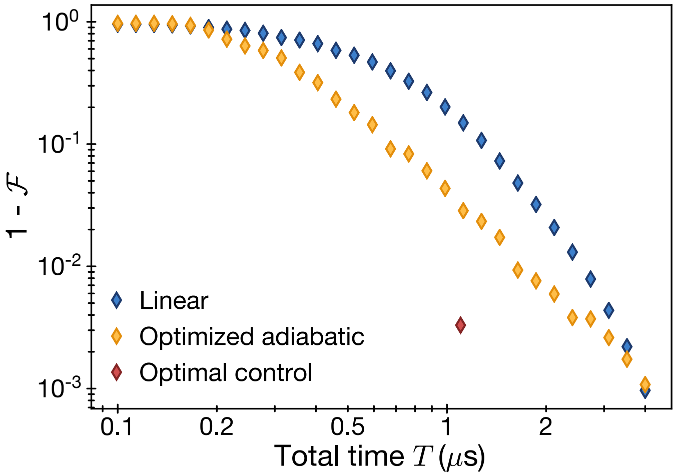

Figure S3: Comparison of ramping profile fidelities. Comparison of linear ramps (blue) to optimized adiabatic ramps (orange) for $N = 12$ as a function of the total ramp time T. The optimal control pulse used in the experiment takes $T = 1.1$ μs and achieves a higher fidelity than either the linear ramp or the optimized adiabatic ramp.

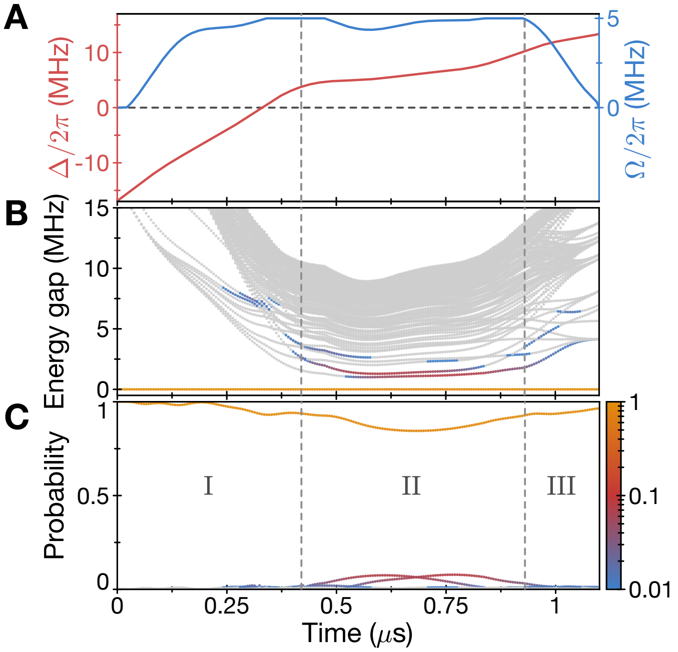

Figure S4: Dynamics of an optimized 20-atom GHZ state preparation. **A,** Optimized control parameters $\Omega(t)$ and $\Delta(t)$ for $N = 20$ atoms. **B,** Energy eigenvalues of instantaneous eigenstates of the Hamiltonian relative to the ground state energy. The population in each energy eigenstate is color coded on a logarithmic scale. Light gray points correspond to populations smaller than 0.01. **C,** Probability in each instantaneous eigenstate as the initial state evolves under the time-dependent Hamiltonian. The probability is dominated by the ground state and a few excited states. The time evolution is computed by exact numerical integration of Schrödinger's equation, and 100 lowest energy eigenstates are obtained by using Krylov subspace method algorithms. For computational efficiency, we only consider the even parity sector of the Hamiltonian with no more than three nearest neighboring Rydberg excitations owing to the Rydberg blockade.

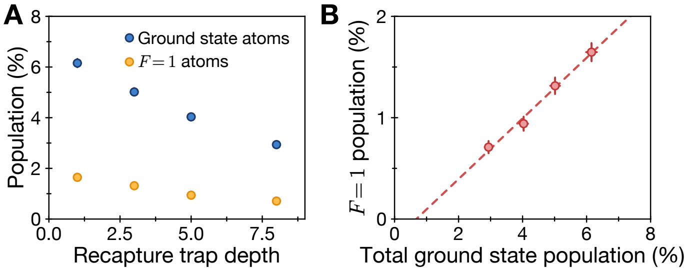

Figure S5: Quantifying detection errors. **A,** Measurement of the recaptured Rydberg atoms in the ground state (blue points) and in the $F = 1$ ground-state manifold (orange points) as a function of the tweezer depth upon recapture. **B,** Recaptured populations in all ground state levels. The intersection with the horizontal axis gives an estimate of the atoms that were not excited to the Rydberg state, bounding the π pulse fidelity.

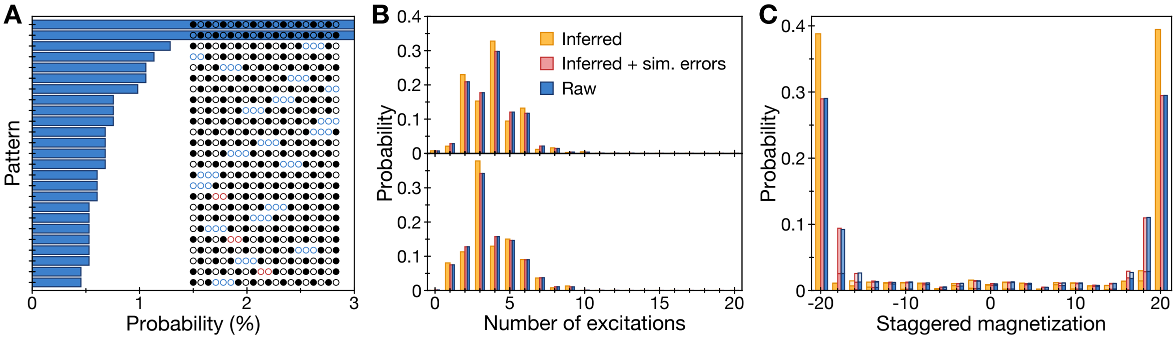

Figure S6: Inference of parity and populations. **A,** Histogram of observed patterns after preparing a 20-atom GHZ state. Open circles denote atoms in $|0\rangle$ and filled circles denote atoms in state $|1\rangle$. Blue domains mark regions where a single detection error has likely occurred, since such patterns are energetically costly at large positive detuning of the Rydberg laser. Red domains mark true domain walls, where the antiferromagnetic order is broken. Following the correct GHZ patterns, the 14 most observed patterns are consistent with a single detection error. **B,** Distribution of number of excitations measured for two different times of the parity oscillation for a 20-atom array, with the upper (lower) plot at $\phi = 0$ ($\phi = \pi/20$) of phase accumulation per atom, showing a net positive (negative) parity. Blue bars show directly measured values, orange bars show the statistically inferred parent distribution, and red bars denote the parent distribution after adding simulated errors to compare to the raw data. **C,** Staggered magnetization M_n extracted from the measurement of GHZ populations for 20 atoms. The vertically split bars with different shading denote different occurrences of number of excitations.

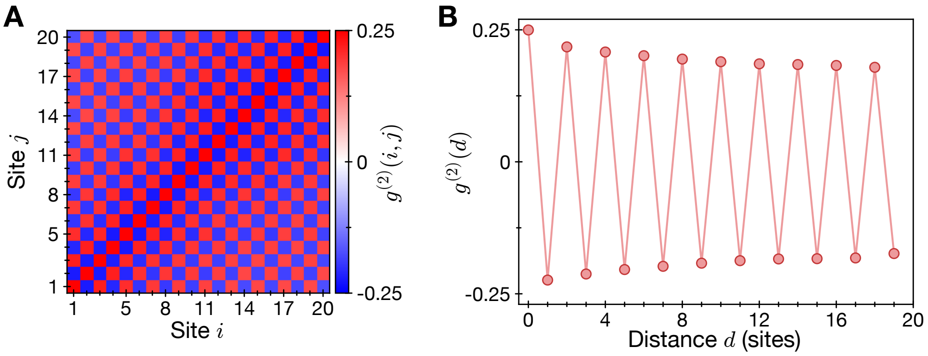

Figure S7: Density-density correlations for a 20-atom GHZ state. **A**, We evaluate the correlation function $g^{(2)}(i,j) = \langle n_i n_j \rangle - \langle n_i \rangle \langle n_j \rangle$ and observe strong correlations of Rydberg excitations across the entire system. **B**, The density-density correlations over distance, given by $g^{(2)}(d) \propto \sum_i g^{(2)}(i,i+d)$ decay only very slowly throughout the array.

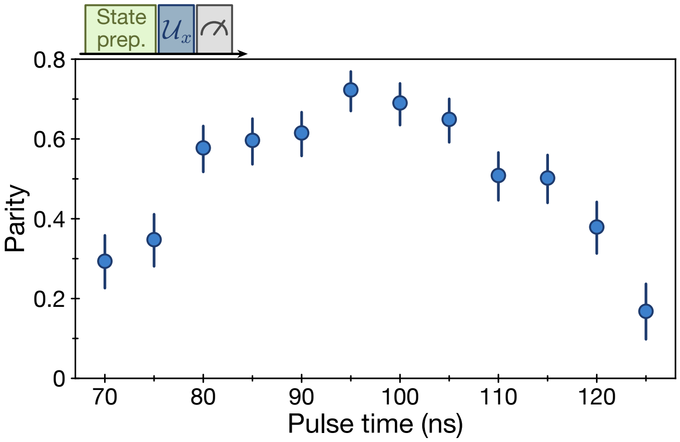

Figure S8: Parity signal measured as a function of the time the operation $\mathcal{U}_x$ is applied. The total time includes delays in the AOM response and the finite laser pulse rise time.

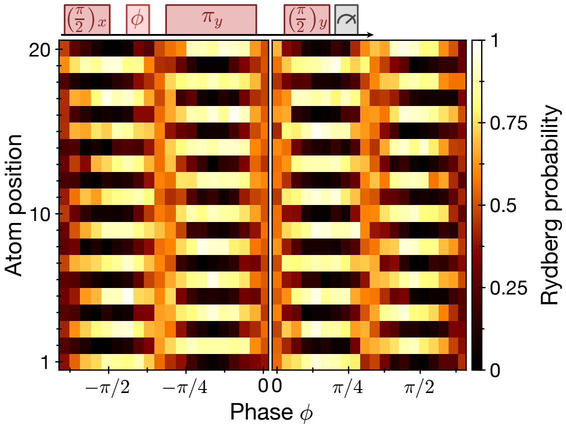

Figure S9: Phase accumulation measured on an array of 20 sites. The left panel demonstrates application of a negative staggered field by applying local addressing beams on the odd sites in the array. The right panel shows a positive staggered field by instead applying local addressing beams on the even sites in the array. Phase is accumulated on each site at a rate of $2\pi \times 3.8$ MHz.

System size N	4	8	12	16	20
Raw populations	0.893(6)	0.797(8)	0.695(9)	0.629(12)	0.585(14)
Inferred	0.946(10)	0.892(17)	0.824(21)	0.791(29)	0.782(32)
Raw coherence	0.710(12)	0.516(11)	0.371(10)	0.282(11)	0.211(11)
Inferred	0.759(11)	0.598(16)	0.462(19)	0.373(19)	0.301(18)
Raw fidelity	0.801(7)	0.657(7)	0.533(7)	0.455(8)	0.398(9)
Inferred	0.852(7)	0.745(12)	0.643(14)	0.582(17)	0.542(18)

Table S1: Measured GHZ data for all system sizes. Errors denote 68% confidence intervals.

References and Notes

1. D. M. Greenberger, M. A. Horne, A. Zeilinger, in *Bell's Theorem, Quantum Theory and Conceptions of the Universe*, M. Kafatos, Ed. (Springer 1989), pp. 69–72.

2. L. Pezzè, A. Smerzi, M. K. Oberthaler, R. Schmied, P. Treutlein, Quantum metrology with nonclassical states of atomic ensembles. *Rev. Mod. Phys.* **90**, 035005 (2018). doi:10.1103/RevModPhys.90.035005

3. M. A. Nielsen, I. L. Chuang, *Quantum Computation and Quantum Information: 10th Anniversary Edition* (Cambridge Univ. Press, ed. 10, 2011).

4. L. Amico, R. Fazio, A. Osterloh, V. Vedral, Entanglement in many-body systems. *Rev. Mod. Phys.* **80**, 517–576 (2008). doi:10.1103/RevModPhys.80.517

5. O. Gühne, G. Tóth, Entanglement detection. *Phys. Rep.* **474**, 1–75 (2009). doi:10.1016/j.physrep.2009.02.004

6. R. Islam, R. Ma, P. M. Preiss, M. E. Tai, A. Lukin, M. Rispoli, M. Greiner, Measuring entanglement entropy in a quantum many-body system. *Nature* **528**, 77–83 (2015). doi:10.1038/nature15750 Medline

7. C. A. Sackett, D. Kielpinski, B. E. King, C. Langer, V. Meyer, C. J. Myatt, M. Rowe, Q. A. Turchette, W. M. Itano, D. J. Wineland, C. Monroe, Experimental entanglement of four particles. *Nature* **404**, 256–259 (2000). doi:10.1038/35005011 Medline

8. R. Laflamme, E. Knill, W. H. Zurek, P. Catasti, S. V. S. Mariappan, NMR Greenberger–Horne–Zeilinger states. *Philos. Trans. R. Soc. London A* **356**, 1941–1948 (1998). doi:10.1098/rsta.1998.0257

9. P. Neumann, N. Mizuochi, F. Rempp, P. Hemmer, H. Watanabe, S. Yamasaki, V. Jacques, T. Gaebel, F. Jelezko, J. Wrachtrup, Multipartite entanglement among single spins in diamond. *Science* **320**, 1326–1329 (2008). doi:10.1126/science.1157233 Medline

10. D. Bouwmeester, J.-W. Pan, M. Daniell, H. Weinfurter, A. Zeilinger, Observation of three-photon Greenberger-Horne-Zeilinger entanglement. *Phys. Rev. Lett.* **82**, 1345–1349 (1999). doi:10.1103/PhysRevLett.82.1345

11. J.-W. Pan, M. Daniell, S. Gasparoni, G. Weihs, A. Zeilinger, Experimental demonstration of four-photon entanglement and high-fidelity teleportation. *Phys. Rev. Lett.* **86**, 4435–4438 (2001). doi:10.1103/PhysRevLett.86.4435 Medline

12. X.-L. Wang, Y.-H. Luo, H.-L. Huang, M.-C. Chen, Z.-E. Su, C. Liu, C. Chen, W. Li, Y.-Q. Fang, X. Jiang, J. Zhang, L. Li, N.-L. Liu, C.-Y. Lu, J.-W. Pan, 18-Qubit entanglement with six photons' three degrees of freedom. *Phys. Rev. Lett.* **120**, 260502 (2018). doi:10.1103/PhysRevLett.120.260502 Medline

13. D. Leibfried, E. Knill, S. Seidelin, J. Britton, R. B. Blakestad, J. Chiaverini, D. B. Hume, W. M. Itano, J. D. Jost, C. Langer, R. Ozeri, R. Reichle, D. J. Wineland, Creation of a six-atom 'Schrödinger cat' state. *Nature* **438**, 639–642 (2005). doi:10.1038/nature04251 Medline

14. T. Monz, P. Schindler, J. T. Barreiro, M. Chwalla, D. Nigg, W. A. Coish, M. Harlander, W. Hänsel, M. Hennrich, R. Blatt, 14-Qubit entanglement: Creation and coherence. *Phys. Rev. Lett.* **106**, 130506 (2011). doi:10.1103/PhysRevLett.106.130506 Medline

15. N. Friis, O. Marty, C. Maier, C. Hempel, M. Holzäpfel, P. Jurcevic, M. B. Plenio, M. Huber, C. Roos, R. Blatt, B. Lanyon, Observation of entangled states of a fully controlled 20-qubit system. *Phys. Rev. X* **8**, 021012 (2018). doi:10.1103/PhysRevX.8.021012

16. L. Dicarlo, M. D. Reed, L. Sun, B. R. Johnson, J. M. Chow, J. M. Gambetta, L. Frunzio, S. M. Girvin, M. H. Devoret, R. J. Schoelkopf, Preparation and measurement of three-qubit entanglement in a superconducting circuit. *Nature* **467**, 574–578 (2010). doi:10.1038/nature09416 Medline

17. C. Song, K. Xu, W. Liu, C. P. Yang, S.-B. Zheng, H. Deng, Q. Xie, K. Huang, Q. Guo, L. Zhang, P. Zhang, D. Xu, D. Zheng, X. Zhu, H. Wang, Y.-A. Chen, C.-Y. Lu, S. Han, J.-W. Pan, 10-qubit entanglement and parallel logic operations with a superconducting circuit. *Phys. Rev. Lett.* **119**, 180511 (2017). doi:10.1103/PhysRevLett.119.180511 Medline

18. B. Vlastakis, G. Kirchmair, Z. Leghtas, S. E. Nigg, L. Frunzio, S. M. Girvin, M. Mirrahimi, M. H. Devoret, R. J. Schoelkopf, Deterministically encoding quantum information using 100-photon Schrödinger cat states. *Science* **342**, 607–610 (2013). doi:10.1126/science.1243289 Medline

19. Materials and methods are available as supplementary materials.

20. H. Labuhn, D. Barredo, S. Ravets, S. de Léséleuc, T. Macrì, T. Lahaye, A. Browaeys, Tunable two-dimensional arrays of single Rydberg atoms for realizing quantum Ising models. *Nature* **534**, 667–670 (2016). doi:10.1038/nature18274 Medline

21. H. Bernien, S. Schwartz, A. Keesling, H. Levine, A. Omran, H. Pichler, S. Choi, A. S. Zibrov, M. Endres, M. Greiner, V. Vuletić, M. D. Lukin, Probing many-body dynamics on a 51-atom quantum simulator. *Nature* **551**, 579–584 (2017). doi:10.1038/nature24622 Medline

22. D. Jaksch, J. I. Cirac, P. Zoller, S. L. Rolston, R. Côté, M. D. Lukin, Fast quantum gates for neutral atoms. *Phys. Rev. Lett.* **85**, 2208–2211 (2000). doi:10.1103/PhysRevLett.85.2208 Medline

23. T. Wilk, A. Gaëtan, C. Evellin, J. Wolters, Y. Miroshnychenko, P. Grangier, A. Browaeys, Entanglement of two individual neutral atoms using Rydberg blockade. *Phys. Rev. Lett.* **104**, 010502 (2010). doi:10.1103/PhysRevLett.104.010502 Medline

24. L. Isenhower, E. Urban, X. L. Zhang, A. T. Gill, T. Henage, T. A. Johnson, T. G. Walker, M. Saffman, Demonstration of a neutral atom controlled-NOT quantum gate. *Phys. Rev. Lett.* **104**, 010503 (2010). doi:10.1103/PhysRevLett.104.010503 Medline

25. R. Islam, C. Senko, W. C. Campbell, S. Korenblit, J. Smith, A. Lee, E. E. Edwards, C.-C. J. Wang, J. K. Freericks, C. Monroe, Emergence and frustration of magnetism with variable-range interactions in a quantum simulator. *Science* **340**, 583–587 (2013). doi:10.1126/science.1232296 Medline

26. N. Rach, M. M. Müller, T. Calarco, S. Montangero, Dressing the chopped-random-basis optimization: A bandwidth-limited access to the trap-free landscape. *Phys. Rev. A* **92**, 062343 (2015). doi:10.1103/PhysRevA.92.062343

27. R. Heck, O. Vuculescu, J. J. Sørensen, J. Zoller, M. G. Andreasen, M. G. Bason, P. Ejlertsen, O. Elíasson, P. Haikka, J. S. Laustsen, L. L. Nielsen, A. Mao, R. Müller, M. Napolitano, M. K. Pedersen, A. R. Thorsen, C. Bergenholtz, T. Calarco, S. Montangero, J. F. Sherson, Remote optimization of an ultracold atoms experiment by experts and citizen scientists. *Proc. Natl. Acad. Sci. U.S.A.* **115**, E11231–E11237 (2018). doi:10.1073/pnas.1716869115 Medline

28. S. de Léséleuc, D. Barredo, V. Lienhard, A. Browaeys, T. Lahaye, Analysis of imperfections in the coherent optical excitation of single atoms to Rydberg states. *Phys. Rev. A* **97**, 053803 (2018). doi:10.1103/PhysRevA.97.053803

29. M. Gärttner, J. G. Bohnet, A. Safavi-Naini, M. L. Wall, J. J. Bollinger, A. M. Rey, Measuring out-of-time-order correlations and multiple quantum spectra in a trapped-ion quantum magnet. *Nat. Phys.* **13**, 781–786 (2017). doi:10.1038/nphys4119

30. E. Farhi, J. Goldstone, S. Gutmann, A quantum approximate optimization algorithm. arXiv:1411.4028 [quant-ph] (2014).

31. L. Zhou, S.-T. Wang, S. Choi, H. Pichler, M. D. Lukin, Quantum approximate optimization algorithm: Performance, mechanism, and implementation on near-term devices. arXiv:1812.01041 [quant-ph] (2018).

32. C. J. Turner, A. A. Michailidis, D. A. Abanin, M. Serbyn, Z. Papić, Weak ergodicity breaking from quantum many-body scars. *Nat. Phys.* **14**, 745–749 (2018). doi:10.1038/s41567-018-0137-5

33. C. J. Picken, R. Legaie, K. McDonnell, J. D. Pritchard, Entanglement of neutral-atom qubits with long ground-Rydberg coherence times. *Quantum Sci. Technol.* **4**, 015011 (2018). doi:10.1088/2058-9565/aaf019

34. C. Song *et al.*, Observation of multi-component atomic Schrödinger cat states of up to 20 qubits. arXiv:1905.00320 [quant-ph] (2019).

35. K. X. Wei *et al.*, Verifying multipartite entangled GHZ states via multiple quantum coherences. arXiv:1905.05720 [quant-ph] (2019).

36. H. Levine, A. Keesling, A. Omran, H. Bernien, S. Schwartz, A. S. Zibrov, M. Endres, M. Greiner, V. Vuletić, M. D. Lukin, High-fidelity control and entanglement of rydberg-atom qubits. *Phys. Rev. Lett.* **121**, 123603 (2018). doi:10.1103/PhysRevLett.121.123603 Medline

37. S. Montangero, T. Calarco, R. Fazio, Robust optimal quantum gates for Josephson charge qubits. *Phys. Rev. Lett.* **99**, 170501 (2007). doi:10.1103/PhysRevLett.99.170501 Medline

38. C. Brif, R. Chakrabarti, H. Rabitz, Control of quantum phenomena: Past, present and future. *New J. Phys.* **12**, 075008 (2010). doi:10.1088/1367-2630/12/7/075008

39. J. Cui, F. Mintert, Robust control of long-distance entanglement in disordered spin chains. *New J. Phys.* **17**, 093014 (2015). doi:10.1088/1367-2630/17/9/093014

40. C. P. Koch, Controlling open quantum systems: Tools, achievements, and limitations. *J. Phys. Condens. Matter* **28**, 213001 (2016). doi:10.1088/0953-8984/28/21/213001 Medline

41. P. Doria, T. Calarco, S. Montangero, Optimal control technique for many-body quantum dynamics. *Phys. Rev. Lett.* **106**, 190501 (2011). doi:10.1103/PhysRevLett.106.190501 Medline

42. S. J. Glaser, U. Boscain, T. Calarco, C. P. Koch, W. Köckenberger, R. Kosloff, I. Kuprov, B. Luy, S. Schirmer, T. Schulte-Herbrüggen, D. Sugny, F. K. Wilhelm, Training Schrödinger's cat: Quantum optimal control. *Eur. Phys. J. D* **69**, 279 (2015). doi:10.1140/epjd/e2015-60464-1

43. I. Brouzos, A. I. Streltsov, A. Negretti, R. S. Said, T. Caneva, S. Montangero, T. Calarco, Quantum speed limit and optimal control of many-boson dynamics. *Phys. Rev. A* **92**, 062110 (2015). doi:10.1103/PhysRevA.92.062110

44. S. Lloyd, S. Montangero, Information theoretical analysis of quantum optimal control. *Phys. Rev. Lett.* **113**, 010502 (2014). doi:10.1103/PhysRevLett.113.010502 Medline

45. S. van Frank, M. Bonneau, J. Schmiedmayer, S. Hild, C. Gross, M. Cheneau, I. Bloch, T. Pichler, A. Negretti, T. Calarco, S. Montangero, Optimal control of complex atomic quantum systems. *Sci. Rep.* **6**, 34187 (2016). doi:10.1038/srep34187 Medline

46. M. M. Müller, A. Kölle, R. Löw, T. Pfau, T. Calarco, S. Montangero, Room-temperature Rydberg single-photon source. *Phys. Rev. A* **87**, 053412 (2013). doi:10.1103/PhysRevA.87.053412

47. T. Caneva, M. Murphy, T. Calarco, R. Fazio, S. Montangero, V. Giovannetti, G. E. Santoro, Optimal control at the quantum speed limit. *Phys. Rev. Lett.* **103**, 240501 (2009). doi:10.1103/PhysRevLett.103.240501 Medline

48. T. Caneva, T. Calarco, R. Fazio, G. E. Santoro, S. Montangero, Speeding up critical system dynamics through optimized evolution. *Phys. Rev. A* **84**, 012312 (2011). doi:10.1103/PhysRevA.84.012312

49. J. Cui, R. van Bijnen, T. Pohl, S. Montangero, T. Calarco, Optimal control of Rydberg lattice gases. *Quantum Sci. Technol.* **2**, 035006 (2017). doi:10.1088/2058-9565/aa7daf

50. J. A. Nelder, R. Mead, A simplex method for function minimization. *Comput. J.* **7**, 308–313 (1965). doi:10.1093/comjnl/7.4.308

51. A. M. Kaufman, B. J. Lester, C. A. Regal, Cooling a single atom in an optical tweezer to its quantum ground state. *Phys. Rev. X* **2**, 041014 (2012). doi:10.1103/PhysRevX.2.041014

52. J. D. Thompson, T. G. Tiecke, A. S. Zibrov, V. Vuletić, M. D. Lukin, Coherence and Raman sideband cooling of a single atom in an optical tweezer. *Phys. Rev. Lett.* **110**, 133001 (2013). doi:10.1103/PhysRevLett.110.133001 Medline

53. V. Khemani, C. R. Laumann, A. Chandran, Signatures of integrability in the dynamics of Rydberg-blockaded chains. *Phys. Rev. B* **99**, 161101 (2019). doi:10.1103/PhysRevB.99.161101

54. W. W. Ho, S. Choi, H. Pichler, M. D. Lukin, Periodic Orbits, Entanglement, and quantum many-body scars in constrained models: Matrix product state approach. *Phys. Rev. Lett.* **122**, 040603 (2019). doi:10.1103/PhysRevLett.122.040603 Medline

55. I. I. Beterov, I. I. Ryabtsev, D. B. Tretyakov, V. M. Entin, Quasiclassical calculations of blackbody-radiation-induced depopulation rates and effective lifetimes of Rydberg n S, n P, and n D alkali-metal atoms with n ≤ 80. *Phys. Rev. A* **79**, 052504 (2009). doi:10.1103/PhysRevA.79.052504